ADVANCED ENGINEERING MATERIALS
www.aem-journal.com

Numerical and Experimental Characterization of Elastic Properties of a Novel, Highly Homogeneous Interpenetrating Metal Ceramic Composite

Dominik Horny, Joél Schukraft, Kay André Weidenmann, and Katrin Schulz*

An interpenetrating aluminum–alumina composite is presented, based on a ceramic foam manufactured via a novel slurry-based route resulting in a highly homogeneous preform microstructure in contrast to other preform techniques. The metal matrix composite (MMC) is produced by infiltrating the open-porous ceramic preform with molten aluminum at 700 °C using a Argon-driven gas pressure infiltration process. The resulting MMC and the primary ceramic foam are investigated both numerically and experimentally in terms of microstructural characteristics. In addition, the mechanical behavior of the material as well as the structural and material interactions on the microscale are investigated. To characterize the MMC regarding mechanical isotropy, elastic properties are determined experimentally via ultrasonic phase spectroscopy (UPS). A fast Fourier transform (FFT) formulation is used to simulate the complex 3D microstructure with reasonable effort based on image-data gathered from high-resolution X-ray computed tomography (CT) scans of the ceramic foam as computational grid. Simulations prove that the material properties are, indeed, considered as highly homogeneous with respect to the material microstructure. A comparison with effective experimental investigations confirms these findings.

1. Introduction

Composite materials usually consist of a continuous phase, referred to as matrix, and one or more reinforcing phases embedded within this matrix.[1] A classification of composite materials can be made in several ways, e.g., according to the matrix material class (polymer, metal, ceramic), according to the reinforcement type (e.g., particles, fibers, whiskers), or according to their manufacturing process (e.g., powder metallurgy, infiltration, stir-casting).[2]

If each phase of the composite is topologically interconnected throughout the whole material volume, it is defined as an interpenetrating phase composite.[3] The interpenetrating microstructure enables each phase to contribute to the macroscopic properties of the composite and also gives the opportunity of developing multifunctional materials.[3,4] Considering a metal–ceramic composite, the most common manufacturing method is to first produce an open-porous ceramic preform and subsequently infiltrate it with the molten metal.

Due to the poor wettability of, e.g., molten aluminum and Al_2O_3 as well as to overcome surface tension, pressure has to be applied to infiltrate the preform. This requires a certain mechanical stability of the ceramic foam and a well-connected open porous network with a sufficiently high permeability.[5] In general, the properties of the resulting interpenetrating metal ceramic composite mainly depend on the architecture and mechanical properties of the ceramic preform.[6] A mechanically stable ceramic framework with dense struts coupled with high (open) porosity >50% and a homogeneous pore size distribution are desired to achieve a high strength of the composite and remain the ductile behaviour of the infiltrated metal.[7] Preforms obtained from pressing and sintering of ceramic powders,[8,9] pore-former processes,[5,10] replica methods,[4,11] gel-casting,[12] freeze-casting,[13,14] or even 3D ink-printing[15] have been used to manufacture interpenetrating metal ceramic composites.

So far, none of these state-of-the-art preform manufacturing methods could fulfill all of the requirements mentioned because they suffer from, e.g., low permeability, lack of homogeneity, and microcracks induced during the decomposition or burnout process (pore-former), remaining closed porosity (additive manufacturing, direct foaming), low mechanical stability (replica), or anisotropy (freeze-casting).[16] In addition, the high manufacturing costs prevent a widespread use of interpenetrating metal matrix composites (MMCs) made from these preforms.[10] Just recently a direct foaming method was found

D. Horny, Dr. K. Schulz
Institute for Applied Materials – Computational Materials Science (IAM-CMS)
Karlsruhe Institute of Technology (KIT)
Strasse am Forum 7, Karlsruhe 76136, Germany
E-mail: dominik.horny@kit.edu

J. Schukraft, Prof. K. A. Weidenmann
Institute of Materials Resource Management (MRM)
University of Augsburg
Universitätsstraße 1, Augsburg 86159, Germany

The ORCID identification number(s) for the author(s) of this article can be found under https://doi.org/10.1002/adem.201901556.

DOI: 10.1002/adem.201901556

enabling a cost-effective manufacturing of ceramic foams showing all the desired features.[17]

This leads to the assumption that it may serve as preform for a cost-efficient, highly homogeneous and mechanically resistant interpenetrating MMC. This assumption is analyzed by the authors in this contribution. In this regard, a porous Al_2O_3 foam produced by mechanical stirring process was infiltrated with AlSi10Mg cast alloy to generate an interpenetrating composite. It has been investigated numerically and experimentally regarding microstructural and elastic properties to analyze its homogeneity, pore size distribution, isotropic elastic behavior, and morphology for structural application under mechanical load.

As composite materials always represent multiscale problems, a large variety of multiscale modeling from nano- to macroscale is used for interpenetrating composites and foam structures.[18–20] The objective of these modeling approaches is to transfer the information gained on a small length scale to a larger length scale in form of effective or homogenized properties to save computation time while remaining the desired accuracy.[21]

For mechanical problems, the well-established finite element method (FEM) is predominantly used to conduct the numerical simulations.[18,20,22–25] For a complex and locally very heterogeneous but globally homogeneous MMC microstructure at hand, an FEM realization needs a very high-resolution grid to account for the different length scales. However, realizing a reasonable computing time requires more efficient methods than the commonly used FEM.[26] Here, spectral methods based on fast Fourier transforms (FFTs) provide an efficient alternative to analyze the complex material microstructures, which enable the efficient computation of complex microstructures discretized on a regular grid avoiding the assembly of a linear system.

In this study, a formulation based on the spectral solver framework of DAMASK[27] is presented to perform the FFT-based microstructure simulations and to discuss the results with respect to the representation by an representative volume element (RVE) approach.

A comparison and validation of the numerical model with the experimental results is presented, and it is shown that the model can be used to predict microstructural material properties and to give meaningful insights into the structural and material interplay. The comparison of experimental and numerical data exhibits that the presented material shows remarkable properties with respect to its homogeneity, isotropy based on a very narrow pore size distribution of the considered preform and a very low residual porosity.

It has to be denoted that although a matrix cannot be uniquely defined for interpenetrating composites we refer to the material as a MMC in the following because the aluminum alloy accounts for the larger volume fraction due to the high open porosity of the preform chosen.

2. Manufacturing the Interpenetrating MMC

State-of-the-art manufacturing techniques of ceramic preforms for interpenetrating alumina–aluminum composites are freeze-casting,[13,14] pore-former processes with pyrolyzable placeholders,[5,10] suspension-based polyurethane system,[4,11,28] and sintering of (coarse) alumina powders to an open-porous ceramic.[8,9] Other methods to get interpenetrating MMCs directly are displacement reaction of silica-glass and molten aluminum[23] or sintering of a mixture of aluminum alloy and alumina powders.[29] In this contribution, the macroscopically homogeneous and highly porous open-cell alumina ceramic preform with an approximate relative density of 25% is produced and provided by Morgan Advanced Materials Haldenwanger GmbH, Waldkraiburg, Germany, which holds a patent on the preform manufacturing process.[30] Here, a slurry-based processing route is used to get a highly homogeneous ceramic preform. By mechanical stirring a stable ceramic foam suspension is produced. By stabilization via additives and a well-engineered drying process, the foam can be mold and dried without losing its fine and homogeneous porosity. By sintering, a ceramic foam as a MMC preform can be produced.

Gas pressure infiltration is used to manufacture the interpenetrating composite. A schematic layout of the apparatus used is shown in **Figure 1**. The ceramic preform is heated in an evacuated vacuum furnace at a residual pressure of 2×10^{-2} mbar with an aluminum slab (AlSi10Mg) up to a maximum temperature of 700 °C. During heating the pressure in the furnace is held between 2×10^{-2} and 10^{-1} mbar. As soon as the maximum temperature is reached and the slab is consequently molten, an external Argon gas pressure of 40 bar is applied onto the surface of the melt covering the previously evacuated preform and the molten aluminum is infiltrated into it. After a short dwell time of 10 min, the chamber is cooled down to room temperature under the remaining Argon pressure. After solidification, the infiltrated preform, i.e., the interpenetrating composite, is removed from the furnace for sample preparation.

3. Experimental Section

To investigate the material experimentally, cubes of the ceramic preform and the MMC were cut out with a diamond wire saw of the infiltrated preform, avoiding surface-near regions to maintain a reproducible sample quality. Cutting was followed by grinding with abrasive SiC grinding paper up to P400 to get parallel surfaces with a final size of the cuboids of $\approx 5 \times 5 \times 5\ mm^3$.

3.1. Density Measurement

To calculate the elastic constants via ultrasound phase spectroscopy (UPS), it was necessary to determine the material density first. The density of the dense MMC was determined using the gas pycnometer AccuPyc II 1340, from Micromertics, Unterschleißheim, Bavaria, Germany in a 10 cm^3 crucible with lid and Helium gas. As this method was not feasible for the open-porous foam, its density was calculated from the mass and the volume of three different Al_2O_3 foam samples (each with a volume of $\approx 90\ cm^3$). The weighing of the samples was performed with an Explorer EX225D, from Ohaus (Nänikon, Zurich, Switzerland) and the volume was measured via micrometer screw gauge.

3.2. Ultrasound Phase Spectroscopy

By nondestructive testing, the elastic constants were determined with UPS method by measuring the velocity of an elastic wave propagating through the investigated material. The method

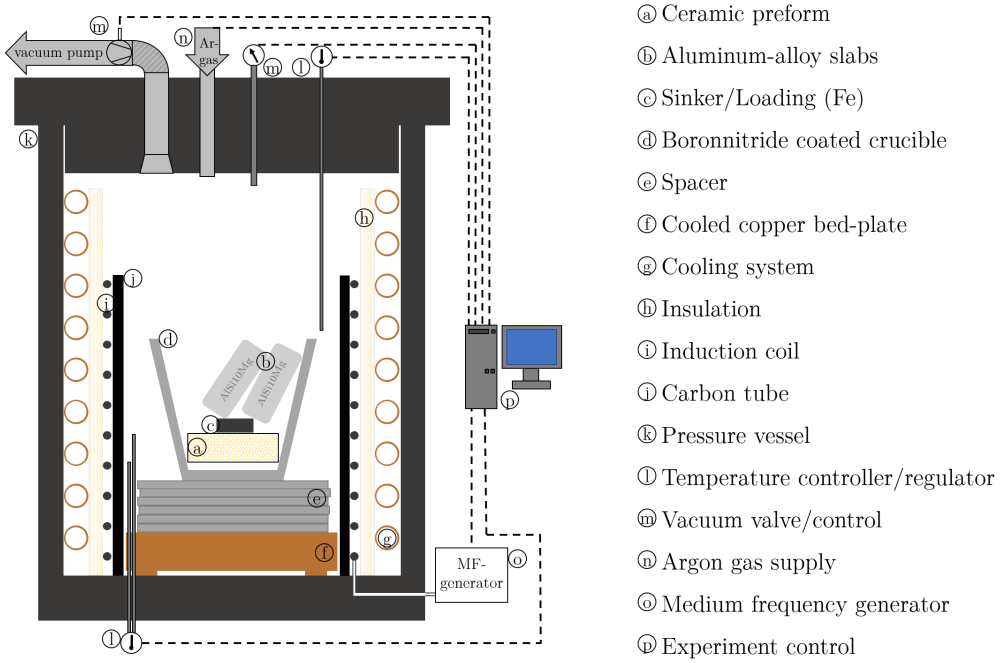

Figure 1. Schematic setting of the gas pressure infiltration with all relevant components.

was described in detail by the following publications[31–34] and had been established for the characterization of the elastic properties of MMCs by Roy et al.[35–37] with the participation of one of the authors of the work presented here. This method was consequently used in this contribution and described in the following. An electronic network analyzer of the type R3754A, Advantest (Tokyo, Japan), connected with a computer with a LabView evaluation software by National Instrument (Austin, Texas, USA) and two pairs of ultrasonic contact transducers (V122-RM, nominal central frequency 7.5 MHz and an oscillator diameter of 9.5 mm for longitudinal waves and V155-RM, nominal central frequency 5 MHz and an oscillator diameter of 12.7 mm for transversal waves, each of Olympus Deutschland GmbH, Hamburg, Germany), was used. As couplant between transducer and specimen commercially available, treacle (Goldsaft by Grafschafter Krautfabrik Josef Schmitz KG, Meckenheim, Germany) was used. The cleaned surface of the transducers was covered with a thin, bubble-free film of the treacle and the specimen was then clamped by springs between the transducers. For each investigated orientation of the cube, the measurement was repeated 3 times and averaged after.

The elastic modulus was calculated from the sample material density and the ratio of the longitudinal and transversal velocities, each measured by UPS. Also, the Poisson's ratio can be calculated from the UPS data. The determination followed from the ratio of the longitudinal and transverse velocities as described elsewhere, like mentioned earlier.

3.3. Microstructure Analysis via X-ray Computed Tomography and Environmental Scanning Electron Microscope

For X-ray computed tomography (CT), a Phoenix nanotom 180 m by GE Sensing & Inspection Technologies GmbH (Wunstorf, Germany) with the software components Phoenix data sx2 acquisition and Phoenix data sx2 reconstruction was used to process the data and reconstruct a 3D image of the sample. Three Al_2O_3 foam cubes, prepared according the aforementioned preparation route and with a size of $\approx 5 \times 5 \times 5$ mm^3, were scanned with the micro-CT. To avoid beam artifacts like beam hardening at the cube edges and stay in a manageable computing time, a representative region of interest (ROI) was chosen of the center of each scanned cube. This ROI was further used for the numerical characterization of the Al_2O_3 foam described in Section 4 and consequently validated regarding the necessary minimum dimensions.

After the AlSi10Mg infiltration of the ceramic foam presented in Section 1, the resulting MMC-cube was scanned additionally to experimentally investigate, e.g., the quality of infiltration, possible destruction of the foam lamellas by the gas pressure infiltration and the residual porosity. Here, VG Studio Max was used to post-process the data and to perform the mentioned analyses. The setting parameters for both the scan of the Al_2O_3 foam and the MMC can be taken out of **Figure 2**b.

For the scanning electron microscopy (SEM) images, an environmental scanning electron microscope (ESEM) of Philips/FEI of the type XL30 with a field-effect transmitter cathode and a beam current of ≈ 140 µA was used. Acceleration voltage, detector type, working distance, magnification, scale, and water vapour pressure in the sample chamber are shown in the respective graphs later.

4. FFT-Based Modeling

FFT-based homogenization of composite materials for linear elastic problems was first introduced by Moulinec and

(a)

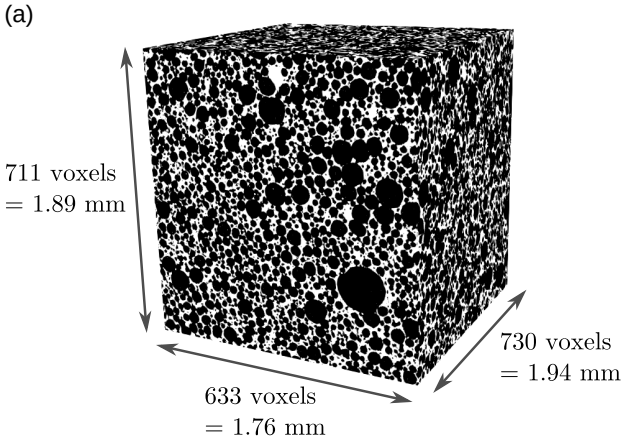

(b)

parameters	unit	Al_2O_3 foam	MMC
voltage	kV	100	80
current	μA	60	180
# of images	-	1000	2000
FOD	mm	8.64	12.5
FDD	mm	325	445
voxelsize	μm^3	2.66^3	2.81^3

Figure 2. a) Binarized micro-CT scan of the Al_2O_3 foam (white = ceramic, black = pore) and b) used paramter settings for the CT scans of the Al_2O_3 foam and the MMC (FOD, focus to object distance; FDD, focus to detector distance).

Suquet[38] in the 1990s. The idea is to approximate the local and overall response of a composite material with Fourier series on an RVE considering periodic boundary conditions. Subjected to an average strain $\bar{\boldsymbol{\varepsilon}}$, the cell problem for the local stresses $\boldsymbol{\sigma}(\mathbf{x})$ and strains $\varepsilon(\mathbf{x})$ (which can be decomposed into the average term $\bar{\varepsilon}$ and a fluctuating part $\tilde{\boldsymbol{\varepsilon}}$ reading $\varepsilon(\mathbf{x}) = \bar{\varepsilon} + \tilde{\varepsilon}(\mathbf{x})$) to be solved is

$$\begin{aligned} &\operatorname{div} \boldsymbol{\sigma}(\mathbf{x}) = \mathbf{0} \\ &\boldsymbol{\sigma}(\mathbf{x}) = \mathbb{C}(\mathbf{x}) : (\bar{\varepsilon} + \tilde{\varepsilon}(\mathbf{x})) \end{aligned} \tag{1}$$

with the locally varying stiffness $\mathbb{C}(\mathbf{x})$. Using an auxiliary problem introducing an isotropic, linear elastic material with stiffness $\mathbb{C}^0$, Equation (1) can be rewritten according to the Lippmann–Schwinger equation as

$$\varepsilon(\mathbf{x}) = -\Gamma^0 * [(\mathbb{C}(\mathbf{x}) - \mathbb{C}^0) : \varepsilon(\mathbf{x})] + \bar{\varepsilon} \tag{2}$$

where Γ^0 is the Green operator associated with $\mathbb{C}^0$ and * is the convolution operator. Equation (2) can subsequently be solved by a fixed point iteration which is also known as the basic scheme.

$$\varepsilon(\mathbf{x})^{i+1} = -\Gamma^0 * [(\mathbb{C}(\mathbf{x}) - \mathbb{C}^0) : \varepsilon(\mathbf{x})^i] + \bar{\varepsilon} \tag{3}$$

It is advantageous to compute the convolution in Fourier space as the operator * becomes an algebraic product and the Green operator Γ^0 is explicitly known in Fourier space. Here, the direct and inverse FFT is used to switch between real and Fourier space to solve discretized problems efficiently.[38,39]

In the past years, FFT methods have been continuously improved in terms of accelerated solvers,[40–42] extension to nonlinear problems,[38] and large deformation formulation.[43] Applications are, e.g., heat conductivity,[40] thermoelasticity,[44] cristal viscoplasticity,[43] void growth,[45] and damage.[46]

In the analyses, in this article, the simulations were performed using the finite strain formulation of the DAMASK framework.[27,43] Here, the fixed point scheme is expressed in terms of deformation gradient $\mathbf{F}$ and first Piola Kirchhoff stress $\mathbf{P}$ using a collocation-based approach at the grid points. For a detailed explanation of the working principle, the choice of the stiffness tensor $\mathbb{C}^0$, the application of mixed boundary conditions, or alternative discretization schemes, we refer to refs. [27,47]. In this study, load boundary conditions are applied by deformation gradient rates and periodic boundary conditions are considered for opposing surfaces of the domains. The resulting equations can be solved iteratively by nonlinear numerical solvers provided by the PETSc (https://www.mcs.anl.gov/petsc/) library.[48] In our simulations, a nonlinear generalized minimal residual method solver was used according to Oosterlee and Washio,[49] following Shanthraj et al.[50] where the efficiency of the solver in combination with the basic collocation approach has been shown. The convergence criterion for the solution is defined by the root mean square (RMS) of the divergence of stress introducing the equilibrium tolerance $\varepsilon_{\text{eq}} = 10^{-10}$ scaled by the length unit m[43]

$$\varepsilon_{\text{eq}} \times m \geq \frac{\text{RMS}(\text{Div}\mathbf{P}(\mathbf{x}))}{\|\bar{\mathbf{P}}\|_2} \tag{4}$$

We model the complex microstructures using the X-ray CT scans. Applying a filtering preprocessing procedure as described in Section 4, the experimental data are directly applied as a computational grid to numerically investigate the elastic material behavior of the ceramic foam and the MMC with the FFT method. The cubic domain is discretized by a regular grids of $N_x \times N_y \times N_z = N \times N \times N = N^3$ wherein every voxel of the CT scan represents an integration point.

5. Microstructural Characterization

5.1. Ceramic Preform

Based on the data from the micro-CT scans described in Section 2, the microstructure of the ceramic foam has been characterized numerically. From the scanned sample ($5 \times 5 \times 5\ mm^3$), a cubic ROI with an edge length of about 1.9 mm located in the center of the sample has been analyzed as a reconstruction volume. To achieve a clear separation between pore and ceramics, which is essential for later numerical simulations, the gray-scale images of the ROI have to be binarized. A global gray-scale

threshold algorithm based on Otsu[51] was used for binarization because the material contrast between the Al_2O_3 and the pores is very high, thus the gray-scale values of the two phases are very different. Subsequently, the pore fraction of the binarized micro-CT scan shown in Figure 2a is determined to be 69.6% by voxel counting.

Nevertheless, the microstructure shown in Figure 2a still shows some segmentation errors, which can be seen more clearly in **Figure 3**a. To guarantee a proper structure for the numerical investigation without artifacts from the reconstruction process, e.g., hovering voxels, and to determine the pore size distribution of the foam, we apply the following postprocessing using the Python scikit-image package:[52] we remove small features to eliminate last remaining segmentation errors by using a combination of erosion with subsequent propagation for both the ceramic and pore volume (see Figure 3a,b). The determination of the pore volume fraction after the image filtering is showing only a 0.03% increase in total porosity compared wth the fractions of the initial binarized scan. Thus, overall porosity is negligibly influenced by the image filtering routine. Then, markers are placed in the middle of the pores using an Euclidean distance transform (EDT) method (see Figure 3c).[53] Finally, a watershed segmentation based on the set markers is applied to distinguish single pores within the connected porous network (Figure 3d).[54]

Considering the almost spherical pore geometry, the pore size is represented by the equivalent sphere radius r which is calculated from the volume V of each segmented pore according to

$$r = \sqrt[3]{\frac{3}{4}\frac{V}{\pi}} \tag{5}$$

The resulting pore size distribution and the calculated generalized extreme value (GEV) probability density function are shown in Figure 3e, and the most important microstructural characteristics of the Al_2O_3 foam are shown in Figure 3f.

This binarized, filtered, and microstructurally characterized micro-CT scan is the basis for the numerical study of the elastic mechanical behavior of both the ceramic foam and the MMC described in Section 5. To get a better understanding of the foam structure, SEM images of the preform are provided (see **Figure 4**c) giving insight in the pore morphology, the interconnection between the pores, and the ceramic struts.

5.2. Composite

The microstructure of the MMC is investigated by X-ray CT to get information about the quality and the completeness of the gas-pressure infiltration as outlined in Section 2. Analyzing the stack of pictures through the whole ROI of each sample, no visible destruction of the ceramic foam lamellae or cracks by expanding the areas of porosity in the ceramic foam by the metal melt can be detected. Including the closed porosity (represented by the black areas) in the ceramic foam, a total residual porosity of 3% is determined. A closer look reveals two main locations of the porosity: spherical casting flaws inside the metal areas on the one hand and residual pores at the ceramic–metal boundary, sickle-shaped in 2D cross section, on the other. The bigger the metallic areas, the bigger are the residual pores in the MMC. Figure 4a,b shows representative cross sections of the micro-CT, respectively. The white spots, spread irregular over the whole image, are image artefacts occurring during the CT. For a even more detailed view regarding the interface between the metal and ceramic component, we refer to the SEM images of the aluminum/Al_2O_3 interface shown in Figure 4d. The interface is dense with some minor flaws due to the shrinkage of the metal during its solidification.

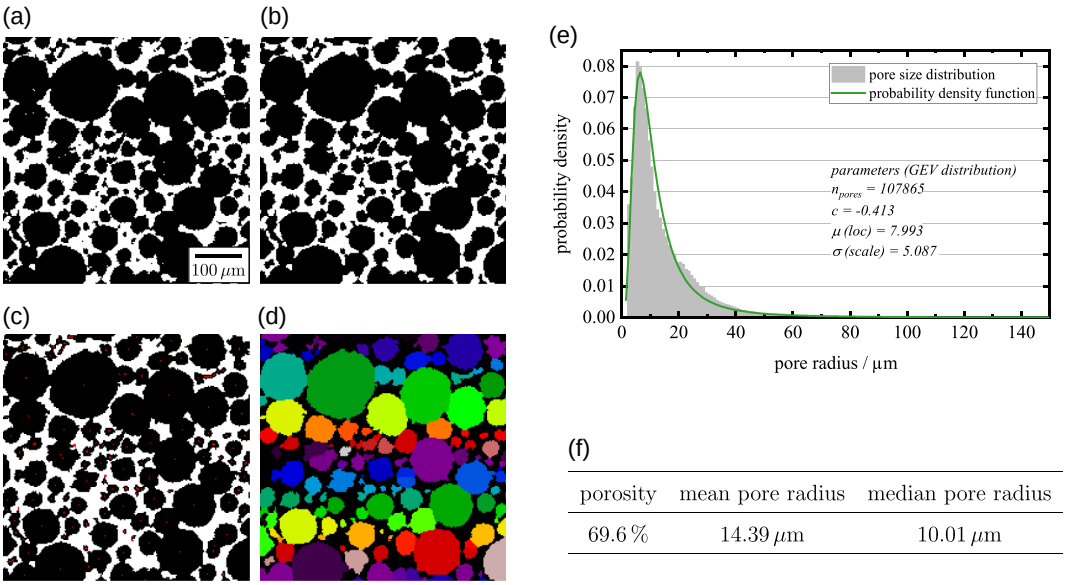

(f)

porosity	mean pore radius	median pore radius
69.6 %	14.39 μm	10.01 μm

Figure 3. Left: Image processing of micro-CT scan images. a) binarized, b) filtered, c) marked by EDT, and d) segmented by watershed algorithm where individual detected pores are identified by different colors. The processes were applied to 3D images, yet 2D images are used here for a descriptive visualization. Right: e) Pore size distribution determined by watershed segmentation of the binarized and filtered micro-CT scan and the derived GEV probability density function with its parameters and f) determined microstructural characteristics of the Al_2O_3 foam.

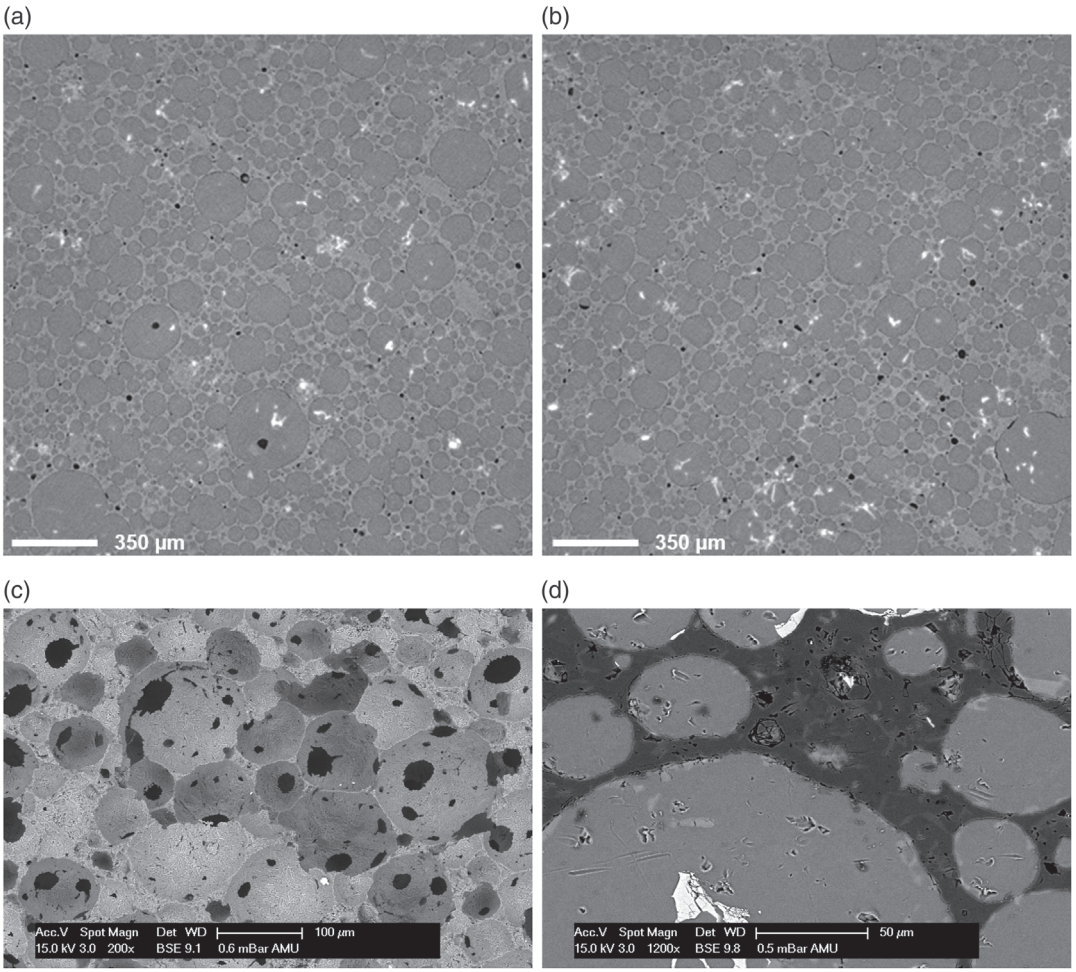

Figure 4. a,b) CT images of representative cross sections indicating the residual porosity of the MMC. c) SEM image of the ceramic foam microstructure prior to infiltration. d) SEM image of the MMC microstructure and internal metal/ceramic interfaces.

6. Determination of Effective Elastic Properties

To determine the effective elastic properties, the Al_2O_3 foam and the MMC material shall be modeled by an RVE. To identify the characteristic size of a statistically meaningful RVE, we choose different sizes of cubic cutouts of the structure with edge lengths from 10 to 100 voxels at 15 randomly chosen points inside of the binarized and filtered 3D scan of the ceramic foam shown in **Figure 5**a. This procedure additionally allows for the validation of the ROI chosen in the micro-CT scan to be representative for the global microstructure.

Subsequently, all of the cubic cutout VEs are analyzed with respect to their ceramic volume fraction. The measured volume fractions dependent on the edge length of the considered cutout are shown in Figure 5b. The average value for each cutout length and the measured ceramic volume fraction of the whole specimen are depicted as well.

Then, the elastic mechanical properties of the materials are investigated by applying a load via a prescribed deformation gradient and calculating the resulting stress response. Here, each voxel of the postprocessed micro-CT scan represents one grid point for the numerical model. As the applied FFT method is not able to exclude material-free volumes (or in other words exclude grid points), it has to be remarked that very low but non-zero stiffness has been assigned to the pore volume in the foam computations.

Assuming an isotropic mechanical behaviour of the single constituents, the following elastic parameters (elastic modulus E and the Poisson's ratio ν) of the primary (dense) Al_2O_3 are taken from the literature,[55,56] resulting in the elastic constants $C_{11,Al_2O_3} = 400.75\,\text{GPa}$ and $C_{12,Al_2O_3} = 100.4\,\text{GPa}$. The elastic constants chosen for the pore volume $C_{11,\text{pore}} = 5.0\,\text{GPa}$ and $C_{12,\text{pore}} = 1.0\,\text{GPa}$ are about a factor of 80 smaller than the ceramic's constants to ensure a minor influence on the overall foam properties. For the MMC modeling, a perfect infiltration of the foam with aluminum is presumed, thus all of the original pore volume is considered to be AlSi10Mg. This is a reasonable assumption regarding the small residual porosity after the infiltration process presented in Section 4. For the aluminum alloy AlSi10Mg, the constants $C_{11,\text{AlSi10Mg}} = 100.2$ and $C_{12,\text{AlSi10Mg}} = 47.1\,\text{GPa}$ were calculated (from E and ν) given by Wu and Harnischmacher.[57,58]

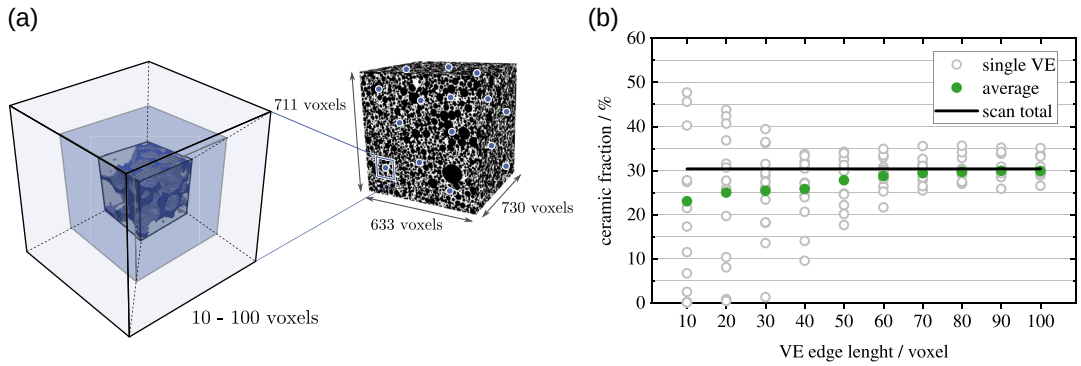

Figure 5. a) Example of cubic cutouts for the RVE study. Volumes from 10^3 to 100^3 voxels were chosen at 15 randomly chosen center points in the filtered micro-CT scan (right, blue dots). In the foam cutout shown in the middle of the box on the left side, the Al_2O_3 is blue and the pore volume is transparent. b) Ceramic fractions of the VEs used for the investigation on effective elastic properties of the foam and the MMC. Green solid dots represent the average value for each VE size. The black line corresponds to the ceramic fraction of the whole micro-CT scan shown in part (a).

A qualitative example of the stress and stain distribution in a 50^3 voxel cutout Al_2O_3 VE under simple uniaxial pressure load is shown in **Figure 6**a.

It can be observed that stresses and strains show local variations due to the microstructure. It is assumed that the average mechanical properties of the VE can be derived from the average stresses $\bar{\boldsymbol{\sigma}}$ and strains $\bar{\varepsilon}$ integrated over the volume V of the respective structure, i.e.

$$\bar{\sigma}_{ij} = \frac{1}{V}\int_V \sigma_{ij}\,\mathrm{d}V \quad \text{and} \quad \bar{\varepsilon}_{ij} = \frac{1}{V}\int_V \varepsilon_{ij}\,\mathrm{d}V \tag{6}$$

The effective stiffness tensor $\bar{\mathbb{C}}$ correlates to the average stresses and strains reading $\bar{\boldsymbol{\sigma}} = \bar{\mathbb{C}} : \bar{\varepsilon}$. Using Voigt notation, the stiffness tensor can be represented as a symmetric 6×6 matrix $\mathbb{C}$ and the second-order tensors as vectors reading

$$\begin{bmatrix} \bar{\sigma}_{11} \\ \bar{\sigma}_{22} \\ \bar{\sigma}_{33} \\ \bar{\sigma}_{23} \\ \bar{\sigma}_{13} \\ \bar{\sigma}_{12} \end{bmatrix} = \begin{bmatrix} C_{11} & C_{12} & C_{13} & C_{14} & C_{15} & C_{16} \\ C_{21} & C_{22} & C_{23} & C_{24} & C_{25} & C_{26} \\ C_{31} & C_{32} & C_{33} & C_{34} & C_{35} & C_{36} \\ C_{41} & C_{42} & C_{43} & C_{44} & C_{45} & C_{46} \\ C_{51} & C_{52} & C_{53} & C_{54} & C_{55} & C_{56} \\ C_{61} & C_{62} & C_{63} & C_{64} & C_{65} & C_{66} \end{bmatrix} \begin{bmatrix} \bar{\varepsilon}_{11} \\ \bar{\varepsilon}_{22} \\ \bar{\varepsilon}_{33} \\ 2\,\bar{\varepsilon}_{23} \\ 2\,\bar{\varepsilon}_{13} \\ 2\,\bar{\varepsilon}_{12} \end{bmatrix} \tag{7}$$

To determine the 36 effective constitutive constant of the matrix $\mathbb{C}$ for the different cutoff volumes, simulations for six independent load cases are applied to the foam structures and to the MMC structures. These are pure compression tests in x(11)-, y(22)-, and z(33)-direction as well as shear tests in yz(23)-, xz(13)-, and xy(12)-direction with disabled strain in the other directions, respectively (see Figure 6b). For all load cases, a constant deformation gradient rate of $\dot{\mathbf{F}} = 5 \times 10^{-4}\,\mathrm{s}^{-1}$ was prescribed for 1 s in the corresponding direction. From the resulting average stress response, one column of $\mathbb{C}$ can be determined for each load case. Then, the effective elastic properties of the foam and the composite are derived from $\mathbb{C}$ with Voigt and Reuss averages[59] as described by Soyarslan et al.[60]

The simulatively derived effective elastic moduli compared with the experimentally determined values for a structure of an edge length of 5 mm are shown in **Figure 7**a for the foam structure and in Figure 7b for the MMC, respectively. The results of the simulatively derived elastic modulus of the foam structure dependent on the ceramic fraction of the considered cutoff is shown in Figure 7c. Here, the size of the considered cutoff is marked in color grades. The results are compared with common analytical composite models, such as the Voigt[61] and Reuss[62]

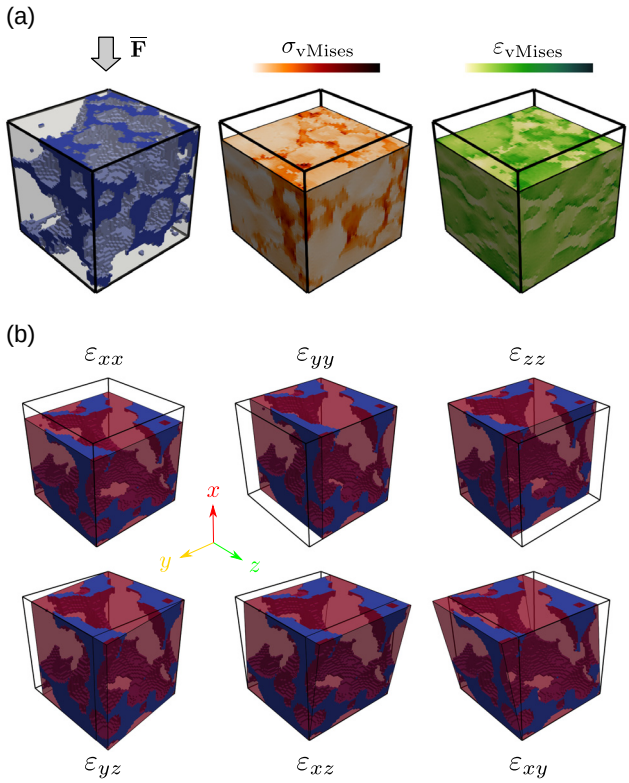

Figure 6. a) 50^3 voxel foam structure under pressure load. Qualitative von Mises stresses and strains resulting from a prescribed compression in x-direction. b) The six independent load cases (pressure in x-, y-, and z-direction and shear in yz-, xz-, and xy-direction) applied to determine the stiffness matrix C of the foam or composite. Here, an MMC of 50 voxel edge length with the Al_2O_3 shown in blue and the AlSi10Mg in transparent red is used as an example.

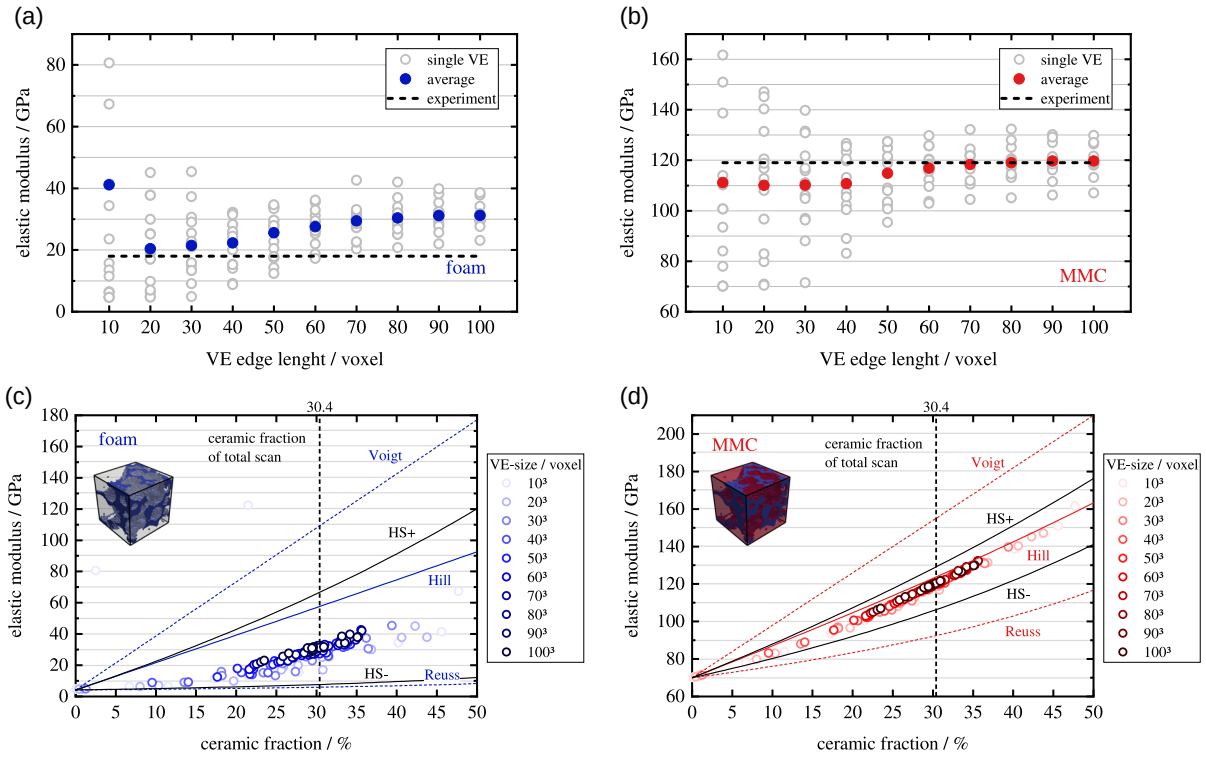

Figure 7. a) Effective elastic Moduli of the investigated VEs for the ceramic foam and b) the MMC, respectively. Fully colored dots represent the average value for each VE size. The dashed line corresponds to the experimentally determined value for a specimen with a ceramic fraction of 30.4%. c) Effective elastic modulus of the foam and d) the MMC applied over of the ceramic fraction of the single VEs. Boundaries of common analytic models for composite materials (Voigt,[66] Reuss,[48] upper (HS+) and lower (HS-) Hashin–Shtrikman,[19] Hill[20]) are presented for comparison.

model considering bounds for axial and transverse loading, the Hashin–Shtrikman upper and lower bounds[63] as well as the Hill model.[59] Analogously, the results of the simulated MMC structure are shown in Figure 7d.

The experimentally determined stiffness coefficients are measured with UPS in the different orientations of the specimen cubes. The measurement follows the method, described by van Buskirk et al.[64] Therefore, the necessary material densities are measured experimentally, like described earlier. The apparent density of the Al_2O_3 foam is 1.01 g cm^{-3} and the density of the MMC is 2.95 g cm^{-3}. The results are opposed to the numerical determined stiffness coefficients in **Table 1**. Here, average values of all 100^3 voxel cutouts are listed.

The results of numerical and experimental determined elastic modulus are shown in Table 1. Also, the Poisson's ratio for the Al_2O_3 foam and the MMC are determined numerically and experimentally. The results are shown in Table 1.

7. Discussion

We introduced a material with an interpenetrating microstructure keeping spherically shaped pores with a mean radius of 14.39 µm. The investigations showed that the material incorporates a particularly high homogeneity with monomodal and narrow pore size distribution as suggested by the preform manufacturing process used. In the literature, ceramic foams and preforms, respectively, are often assumed to be approximately homogeneous without proof and pore morphology is quantified only by a mean pore/cell and window size or a pores

Table 1. Determined stiffness coefficients (C_{ij}), elastic moduli (E_{ij}), and Poisson's ratios (ν) of the Al_2O_3 foam and the MMC. The numerical results shown are average values of all simulated 100^3 voxel structures. The experimental values marked with * are calculated from the other experimentally determined elastic parameters, assuming isotropic material behavior. All values are given in GPa (except of ν which has no unit).

		C_{11}	C_{22}	C_{33}	C_{44}	C_{55}	C_{66}	C_{12}	C_{13}	C_{23}	E_{11}	E_{22}	E_{33}	E_{eff}	ν
Al_2O_3	Exp	30.2	29.8	28.5	7.2	6.7	6.6*	17.0*	17.0*	17.0*	19	19	15	18	0.36
	Num	33.7	35.2	37.8	13.6	12.8	12.0	8.8	8.9	9.0	30	31	33	31	0.21
MMC	exp	154.1	149.5	153.5	46.2	45.0	45.7*	63.2*	63.2*	63.2*	117	117	112	118	0.29
	num	152.0	152.9	155.0	47.2	46.7	46.1	59.7	59.5	59.6	119	119	121	120	0.28

per inch (ppi) value. However, in many cases fabrication methods already induce certain heterogeneity or directed microstructural distributions. In this study, homogeneity of the foam has been proven by determining a well-defined distribution. Pore sizes vary within one order of magnitude, thus they are comparable to foams produced, e.g., by replica methods which are considered to be homogeneous.[65] However, the relatively small mean pore radius compared with other foams used for liquid metal infiltration[4,28,66,67] is advantageous as investigations have shown superior mechanical behaviour for microporous foams. This is assumed to positively affect the properties of the MMCs produced therefrom. Acchar et al.[68] determined an approximately 1.5 times higher flexural strength for a 40 ppi (≈1.4 MPa) compared with a 10 ppi replica foam (≈0.8 MPa). Furthermore, Colombo and Bernardo[69] found that microcellular foams (8 μm cell size) made from preceramic polymers show a 2–5 times higher compression strenght than macrocellular foams (100–600 μm cell size) with similar density of the ceramic struts (e.g., 19 MPa vs 4 MPa for a bulk density of approximately 0.45 g cm^{-3}).

Based on the applied filtering methods, the foam and MMC structures can be efficiently modeled using a FFT method. Analyzing the microstructure with respect to the ceramic volume fraction (Figure 5b), it is found that starting from an RVE edge length of about 160 μm (or 60 voxels) the structure yields a stable ceramic fraction of approximately 30%. This finding underlines the high homogeneity of the preform and the MMC, respectively, as well as the representative character, i.e., size of the region of interest chosen within the cuboid sample.

Comparing the effective elastic properties for this RVE size shows that the effective elastic modulus derived by simulations corresponds well with the experimental values of the MMC (Figure 7b). Here, the FFT modeling technique yields reasonable insights and a robust as well as efficient computational method for the analysis of the locally heterogeneous MMC microstructures based on micro-CT scans. The results in Figure 7d show that the effective elastic modulus can be approximated by Hill's model based on the ceramic fraction. The different sizes and topologies of the single cutoff microstructures have only minor impacts on the results compared with the ceramic fraction of the VEs. This finding shows that the important microstructural features can be captured even for very small cutouts volume, which again indicates a high homogeneity of the material. Considering these insights, we can confirm the choice of our ROI size to be sufficiently large because it captures the materials overall ceramic fraction. However, a definite RVE might not yet be found even for a 100^3 voxel VE size.

For the ceramic foam structure, the results for the effective elastic modulus obtained from simulations exceed the measured values (see Figure 7a,c). This might be because that a small but nonzero stiffness has been assigned to the pore volume. A slight stiffening might also come in due to free surfaces that cannot be modeled with the chosen method because neighboring nodes/integration points are always considered to be perfectly bonded. This leads to an overestimation of the stiffness in the numerical studies of the foam. Furthermore, the results for the effective values of the chosen cutoff structures show larger scattering, especially for small VEs. However, this behaviour can be expected due to the larger stiffness contrast of the ceramic and the pore fractions. Small variations in the ceramic fraction and its geometrical arrangement can have an influence on the elastic properties. For very small cutoffs, it is possible that only a small number or even no connected ceramic paths exist in one or several directions of the investigated RVE. This would result in a very low stiffness in the corresponding direction, although the overall ceramic fraction does not necessarily has to be small. This effect might occur even stronger for shear load due to the FFT voxel discretization of the structure because neighboring hexahedral elements are connected only via the surfaces. To transmit stress in a direction diagonally to the coordinate axes, a ceramic connection of at least two voxels is needed. Otherwise, the properties are pore-dominated. To minimize this effect, a significantly higher voxel resolution could be chosen for the simulation. However, the impact of such geometric characteristics is observed just for the foam structure. The smaller difference of the elastic constants of the composite material and the "support" of the aluminum matrix significantly reduces this effect and is negligibly small in the present observation.

The experimental microstructural investigations proof the completeness of the infiltration process of the composite and attest the fitting infiltration parameters for the gas-pressure infiltration. Merely casting defects inside of bigger areas of metal and at the phase boundary can be detected. These can be explained by the density difference of the infiltrated metal melt and the afterward solidified metal matrix (shrinkage effects). The contraction of the metal matrix during solidification can either lead to an interfacial debonding which causes the sickle-shaped pores in the cross section pictures at the phase boundaries or to casting flaws as seen inside the metal phase. In addition, the preform may feature some closed-cell porosity due to the manufacturing process. With a total residual porosity of about 3%, there are other materials showing slightly lower residual porosity, as, e.g., Prielipp et al.,[29] who quote a porosity of 1% for their pore-former-based ceramic foam composite. However, their ceramic content is almost twice as high as in the present material. Merzkirch et al.[14] quote a residual porosity of up to 1.7% for their freeze-casted alumina/aluminum MMC. However, they use a method to determine open porosity only. Gil et al., e.g., used a ceramic foam with comparable porosity for infiltration.[70] The microstructure of the foam shows different disadvantages, like a large portion of 4.6% closed porosity in the ceramic foam with 74% porosity. Also, the microstructure of the foams they used is difficult to infiltrate because of small pores with a significant volume portion within the cell walls, which are just connected by fine branched pore channels. To infiltrate the whole open porosity under respect of these microstructural aspects, an infiltration pressure of 103 bar is necessary. The results in the present article show that a satisfying result of infiltration with the microstructure of the ceramic preform used in thisarticle, with only 40 bar infiltration pressure can be achieved. In the article of Dolata, the microstructural influence of the manufacturing technique of porous struts becomes obvious.[11] In comparison with their ceramic preform, the compact and dense cell walls of the ceramic foam used in this studies are shown. These examples show the significance of the microstructure of the ceramic preform for a successful development of an interpenetrating MMC.

For the investigations of elastic properties, the numerical results proof in comparison with the experiment a minor impact of the residual porosity. This can be seen from the comparison of numerical and experimental data in Table 1, as the elastic properties only differ by a maximum of 2%. An almost perfectly isotropic behavior of both the foam and the MMC was determined in the experiments and in the simulations emphasizing the high homogeneity of the ceramic preform as well as the good quality of AlSi10Mg infiltration.

The MMC with a ceramic fraction of 30.4% shows an effective elastic modulus of approximately 120 GPa. As the preform chosen has not been used for the manufacturing of interpenetrating composites before, just a small number of investigations with at least similar composite constituents, fractions, and architectures can be considered for a comparison of the elastic properties. However, as our numerical investigations yield a clear dependence of elastic properties on ceramic fraction, a comparison with other interpenetrating aluminum/alumina composites with similar volume fractions can be made. Peng et al. determined elastic moduli of almost 110 GPa for a composite made from 6061 aluminum alloy and a ceramic volume fraction of ≈22.5%.[4] Roy et al.[35] and Moon et al.[71] found elastic moduli of 140–156 and 135 GPa, respectively, for pore-former-based alumina preform MMCs with a ceramic content of approximately 35% and an AlSi12 aluminum alloy metal matrix.

The elastic properties of the material introduced in our study are comparable with the values published in the literature considering the corresponding ceramic contents. However, to the best knowledge of the authors, the highly isotropic behavior even on a small length scale has not been reached for interpenetrating alimunum/alumina composites so far. Therefore, superior properties of the investigated material are expected beyond the elastic range and will be subject to further investigations.

8. Conclusion

The MMC material has been investigated including the characterization of its slurry-based, open-cell ceramic preform. Based on the acquired CT data including the morphology and microstructure of the ceramic preform, the investigations on the elastic properties and characterization of the material were taken parallel in an experimental and numerical study. By establishing a suitable model, the elastic properties of the ceramic preform and the infiltrated MMC could be simulated as well as dependencies of the behavior of the composite and the influences in scale of the investigated VE. Experimental investigations were taken on the infiltration of the ceramic preform via gas pressure infiltration with the aluminum alloy AlSi10Mg and the determination on the elastic behavior of the ceramic preform as well as the MMC.

It has been shown that the numerical material model provides reasonable results for the MMC. The experimental data could be reproduced accurately and thus allow for meaningful insights into the complex microstructure. The numerical investigations on the RVE size showed a stabilization of the results to a certain range of values for cubes with an edge length of ≈160 µm. The values are stable and reproducible for a similar ratio of ceramic–metal volume fractions in the compared representative volumes. This also showed the sufficient size of the ROI taken for the CT investigations.

Closer investigations on increasing VEs might bring scientific findings on a definite RVE. Yet, as the major influence of the ceramic fraction has been shown in this study, a smaller VE size with the right material fractions is perfectly sufficient to determine the effective elastic properties, and furthermore, more efficient considering computational time. With the numerial model other morphologies of ceramic preforms as well as other material combinations can be investigated. For example, RVE microstructures can be generated by computational methods and further be used to optimize the microstructure itself by systematically varying, i.e., the pore size distribution or morphology.

The well-consistent results of numerical and experimental investigation proved the choice of suited parameters for the gas pressure infiltration. The small amount of residual porosity did not carry weight for the elastic properties. It has been found that the novel MMC material follows the Hill model quite accurately and therefore showed also locally a highly homogeneous elastic behavior. This supports the investigations on the elastic properties that showed a strongly isotropic behavior of the MMC as a result of the highly homogeneous ceramic preform used. Furthermore, the narrow pore size distribution and small mean pore size of the preform promise superior properties for the mechanical application of the MMC.

A next step of experimental and numerical investigations on the novel material will be the investigation of the properties beyond the elastic range. Here, the residual porosity might play a significant role. Therefore, a reduction of the residual porosity is an achievable goal: higher pressure for gas pressure infiltration can show if casting defects are reducible/avoidable.

Acknowledgements

The financial support for this work in the context of the DFG research projects SCHU 3074/1-1 and WE 4273/17-1 as well as the support by the European Social Fund and the State Baden-Württemberg is gratefully acknowledged. The authors thank Morgan Advanced Materials Haldenwanger GmbH for the friendly supply of complimentary preform material.

Conflict of Interest

The authors declare no conflict of interest.

Keywords

elastic properties, fast Fourier transform, interpenetrating phase composites, microstructural characterization, representative volume elements, ultrasonic phase spectroscopy

Received: December 20, 2019
Revised: March 15, 2020
Published online: May 4, 2020

[1] K. K. Chawla, *Composite Materials*, Springer, New York, NY **2012**.
[2] A. Mortensen, J. Llorca, *Annu. Rev. Mater. Res.* **2010**, *40*, 243.
[3] D. R. Clarke, *J. Am. Ceram. Soc.* **1992**, *75*, 739.

[4] H. X. Peng, Z. Fan, J. R. Evans, *Mater. Sci. Eng. A* **2001**, *303*, 37.
[5] A. Mattern, B. Huchler, D. Staudenecker, R. Oberacker, A. Nagel, M. J. Hoffmann, *J. Eur. Ceram. Soc.* **2004**, *24*, 3399.
[6] E. C. Hammel, O. L. Ighodaro, O. I. Okoli, *Ceram. Int.* **2014**, *40*, 15351.
[7] O. Ulrich, PhD Thesis, Karlsruhe Institute of Technology **2012**.
[8] N. A. Travitzky, *J. Mater. Sci.* **2001**, *36*, 4459.
[9] K. Konopka, M. Szafran, *J. Mater. Process. Technol.* **2006**, *175*, 266.
[10] F. Scherm, R. Völkl, A. Neubrand, F. Bosbach, U. Glatzel, *Mater. Sci. Eng. A* **2010**, *527*, 1260.
[11] A. J. Dolata, *J. Mater. Eng. Perform.* **2016**, *25*, 3098.
[12] J. Binner, H. Chang, R. Higginson, *J. Eur. Ceram. Soc.* **2009**, *29*, 837.
[13] S. Roy, J. Gibmeier, K. A. Weidenmann, A. Nagel, A. Wanner, *Materials Challenges and Testing for Manufacturing, Mobility, Biomedical Applications and Climate* (Eds: W. Udomkichdecha, T. Böllinghaus, A. Manonukul, J. Lexow), Springer International Publishing, Cham **2014**, p. 77.
[14] M. Merzkirch, Y. Sinchuk, K. A. Weidenmann, R. Piat, *Developments in Strategic Ceramic Materials*, Vol. *10* (Eds: W. M. Kriven, J. Wang, D. Zhu, T. Fischer, S. Kirihara), John Wiley & Sons, Hoboken, NJ **2015**, p. 153.
[15] C. San Marchi, M. Kouzeli, R. Rao, J. A. Lewis, D. C. Dunand, *Scr. Mater.* **2003**, *49*, 861.
[16] A. Mattern, PhD Thesis, Universität Karlsruhe (TH) **2004**.
[17] O. Lavrentyeva, PhD Thesis, Universität Bremen **2006**.
[18] P. Kanouté, D. P. Boso, J. L. Chaboche, B. A. Schreer, *Arch. Comput. Methods Eng.* **2009**, *16*, 31.
[19] J. Llorca, C. González, J. M. Molina-Aldareguía, J. Segurado, R. Seltzer, F. Sket, M. Rodríguez, S. Sádaba, R. Muñoz, L. P. Canal, *Adv. Mater.* **2011**, *23*, 5130.
[20] E. Hamed, E. Novitskaya, J. Li, P. Y. Chen, I. Jasiuk, J. McKittrick, *ActaBiomater.* **2012**, *8*, 1080.
[21] B. Engquist, X. Li, W. Ren, W. E., *Commun. Comput. Phys.* **2007**, *2*, 367.
[22] V. Kouznetsova, W. A. M. Brekelmans, F. P. T. Baaijens, *Comput. Mech.* **2017**, *27*, 1.
[23] G. S. Daehn, B. Starck, L. Xu, K. F. Elfishawy, J. Ringnalda, H. L. Fraser, *Acta Mater.* **1996**, *44*, 249.
[24] R. Jhaver, H. Tippur, *Mater. Sci. Eng. A* **2009**, *499*, 507.
[25] Z. Poniznik, V. Salit, M. Basista, D. Gross, *Comput. Mater. Sci.* **2008**, *44*, 813.
[26] J. Zeman, T. W. de Geus, J. Vondřejc, R. H. Peerlings, M. G. Geers, *Int. J. Numer. Methods Eng.* **2017**, *111*, 903.
[27] F. Roters, M. Diehl, P. Shanthraj, P. Eisenlohr, C. Reuber, S. L. Wong, T. Maiti, A. Ebrahimi, T. Hochrainer, H. O. Fabritius, S. Nikolov, M. Friák, N. Fujita, N. Grilli, K. G. Janssens, N. Jia, P. J. Kok, D. Ma, F. Meier, E. Werner, M. Stricker, D. Weygand, D. Raabe, *Comput. Mater. Sci.* **2019**, *158*, 420.
[28] H. X. Peng, Z. Fan, J. R. G. Evans, J. J. C. Busfield, *J. Eur. Ceram. Soc.* **2000**, *20*, 807.
[29] H. Prielipp, M. Knechtel, N. Claussen, S. K. Streiffer, H. Müllejans, M. Rühle, J. Rödel, *Mater. Sci. Eng. A* **1995**, *197*, 19.
[30] O. Lavrentyeva (Morgan Advanced Materials Haldenwanger GmbH), *DE102015202277A* **2016**.
[31] L. C. Lynnworth, E. P. Papadakis, W. R. Rea, in *Ultrasonic Symp.* IEEE, Monterrey, CL, **1973**, p. 533.
[32] C. S. Ting, W. Sachse, *J. Acoust. Soc. Am.* **1978**, *64*, 852.
[33] L. C. Lynnworth, W. R. Rea, E. P. Papadakis, *J. Acoust. Soc. Am.* **1981**, *70*, 1699.
[34] A. Wanner, *Mater. Sci. Eng. A* **1998**, *248*, 35.
[35] S. Roy, O. Stoll, K. A. Weidenmann, A. Nagel, A. Wanner, *Compos. Sci. Technol.* **2011**, *71*, 962.
[36] S. Roy, K. G. Schell, E. C. Bucharsky, P. Hettich, S. Dietrich, K. A. Weidenmann, A. Wanner, M. J. Hoffmann, *J. Am. Ceram. Soc.* **2012**, *95*, 3078.
[37] S. Roy, K. G. Schell, E. C. Bucharsky, K. A. Weidenmann, A. Wanner, M. J. Hoffmann, *J. Am. Ceram. Soc.* **2013**, *96*, 2269.
[38] H. Moulinec, P. Suquet, *Comput. Methods Appl. Mech. Eng.* **1998**, *157*, 69.
[39] H. Moulinec, P. Suquet, *Phys. B Condens. Matter* **2003**, *338*, 58.
[40] D. J. Eyre, G. W. Milton, *EPJ. Appl. Phys.* **1999**, *6*, 41.
[41] J. C. Michel, H. Moulinec, P. Suquet, *Comput. Model. Eng. Sci.* **2000**, *1*, 79.
[42] J. Zeman, J. Vondřejc, J. Novák, I. Marek, *J. Comput. Phys.* **2010**, *229*, 8065.
[43] P. Eisenlohr, M. Diehl, R. A. Lebensohn, F. Roters, *Int. J. Plast.* **2013**, *46*, 37.
[44] V. Vinogradov, G. W. Milton, *Int. J. Numer. Methods Eng.* **2008**, *76*, 1678.
[45] R. A. Lebensohn, J. P. Escobedo, E. K. Cerreta, D. Dennis-Koller, C. A. Bronkhorst, J. F. Bingert, *Acta Mater.* **2013**, *61*, 6918.
[46] D. Wang, P. Shanthraj, H. Springer, D. Raabe, *Mater. Des.* **2018**, *160*, 557.
[47] P. Shanthraj, M. Diehl, P. Eisenlohr, F. Roters, D. Raabe, *Handbook of Mechanics of Materials* (Eds: C.-H. Hsueh, S. Schmauder, C.-S. Chen, K. K. Chawla, N. Chawla, W. Chen, Y. Kagawa), Springer, Singapore **2019**, p. 1.
[48] S. Balay, S. Abhyankar, M. Adams, J. Brown, P. Brune, K. Buschelman, L. Dalcin, A. Dener, V. Eijkhout, W. Gropp, D. Karpeyev, D. Kaushik, M. Knepley, D. May, L. Curfman McInnes, R. Mills, T. Munson, K. Rupp, P. Sanan, B. Smith, S. Zampini, H. Zhang, H. Zhang, *PETSc Users Manual*, ANL-95/11–Revision 3.12, Argonne National Laboratory **2019**.
[49] C. W. Oosterlee, T. Washio, *SIAM J. Sci. Comput.* **2000**, *21*, 1670.
[50] P. Shanthraj, P. Eisenlohr, M. Diehl, F. Roters, *Int. J. Plast.* **2015**, *66*, 31.
[51] N. Otsu, *IEEE Trans. Syst. Man Cybern.* **1979**, *9*, 62.
[52] S. Van Der Walt, J. L. Schönberger, J. Nunez-Iglesias, F. Boulogne, J. D. Warner, N. Yager, E. Gouillart, T. Yu, *PeerJ* **2014**, *2014*, 1.
[53] R. Fabbri, L. Da, F. Costa, J. C. Torelli, O. M. Bruno, *ACM Comput. Surv.* **2008**, *40*, 41.
[54] P. Soille, M. Ansoult, *Signal Process.* **1990**, *20*, 171.
[55] R. Coble, W. Kingery, *J. Am. Ceram. Soc.* **1954**, *37*, 107.
[56] R. Munro, *J. Am. Ceram. Soc.* **1997**, *28*, 1919.
[57] J. Wu, L. Wang, X. An, *Optik* **2017**, *137*, 65.
[58] A. Harnischmacher, PhD Thesis, Karlsruhe Institute of Technology **2013**.
[59] R. Hill, *Proc. Phys. Soc.* **1952**, *65*, 349.
[60] C. Soyarslan, S. Bargmann, M. Pradas, J. Weissmüller, *Acta Mater.* **2018**, *149*, 326.
[61] W. Voigt, *Lehrbuch der Kristallphysik*, Vieweg+Teubner, Wiesbaden **1966**.
[62] A. Reuss, *Z. Angew. Math. Mech.* **1929**, *9*, 49.
[63] Z. Hashin, S. Shtrikman, *J. Mech. Phys. Solids* **1963**, *11*, 127.
[64] W. C. van Buskirk, S. C. Cowin, R. N. Ward, *J. Biomech. Eng.* **1981**, *103*, 67.
[65] E. Maire, P. Colombo, J. Adrien, L. Babout, L. Biasetto, *J. Eur. Ceram. Soc.* **2007**, *27*, 1973.
[66] P. Colombo, *J. Eur. Ceram. Soc.* **2008**, *28*, 1389.
[67] M. W. Kennedy, K. Zhang, R. Fritzsch, S. Akhtar, J. A. Bakken, R. E. Aune, *Metall. Mater. Trans. B Process Metall. Mater. Process. Sci.* **2013**, *44*, 671.
[68] W. Acchar, E. G. Ramalho, F. B. Souza, W. L. Torquato, V. P. Rodrigues, M. D. Innocentini, *J. Mater. Sci.* **2008**, *43*, 6556.
[69] P. Colombo, E. Bernardo, *Compos. Sci. Technol.* **2003**, *63*, 2353.
[70] R. Gil, A. Jinnapat, A. R. Kennedy, *Compos. A Appl. Sci. Manuf.* **2012**, *43*, 880.
[71] R. J. Moon, M. Tilbrook, M. Hoffman, A. Neubrand, *J. Am. Ceram. Soc.* **2005**, *88*, 666.